Article

Not peer-reviewed version

Enabling Passive Load-Holding Function and System Pressures Control in a One-Motor-One-Pump Motor-Controlled Hydraulic Cylinder: Simulation Study

Wei Zhao *, Morten Kjeld Ebbesen, Michael Rygaard Hansen, Torben Ole Andersen

Posted Date: 11 April 2024

doi: 10.20944/preprints202404.0809.v1

Keywords: Motor-controlled hydraulic cylinder; four-quadrant operation; system pressures control; passive load-holding function

Article

Enabling Passive Load-Holding Function and System Pressures Control in a One-Motor-One-Pump Motor-Controlled Hydraulic Cylinder: Simulation Study

Wei Zhao [1,*], Morten Kjeld Ebbesen [1], Michael Rygaard Hansen [1] and Torben Ole Andersen [2]

[1] Department of Engineering Sciences, University of Agder, 4879 Grimstad, Norway; michael.r.hansen@uia.no (M.R.H); morten.k.ebbesen@uia.no (M.K.E)
[2] Department of Energy Technology, Aalborg University, 9220 Aalborg East, Denmark; toa@energy.aau.dk
* Correspondence: wei.zhao@uia.no

Abstract: This paper is concerned with a hydraulic cylinder directly controlled by a variable speed fixed displacement pump. The considered configuration is referred to as a one-motor-one-pump (1M1P) motor-controlled hydraulic cylinder (MCC). A 1M1P MCC with a hydraulically driven passive load-holding function enabled by controlled system pressures is proposed. The proposed load-holding functionality works if there is a standstill command, a loss of power supply, or a hose rupture. Additionally, this paper conducts a comprehensive analysis of the proposed system's operation and load-holding function across four quadrants. Simulation results demonstrate the four-quadrant operation and good load-holding performance under the aforementioned scenarios. In conclusion, the proposed 1M1P MCC can be successfully used on practical applications characterized by overrunning loads and four quadrant operation.

Keywords: motor-controlled hydraulic cylinder; four-quadrant operation; system pressures control; passive load-holding function

---

1. Introduction

The valve-controlled hydraulic cylinder (VCC) is used extensively in various industries, particularly in heavy load-carrying scenarios. VCCs offer numerous advantages, including a high power-to-weight ratio, flexible power transmission, inherent damping qualities, and a good liability. Despite decades of development, VCCs still face a major challenge: valve throttling losses. These losses are mainly from the system's control and overcenter valves [1]. For instance, control valves account for approximately 29 % to 35 % of the total energy losses in an excavator equipped with load-sensing functionality [2,3]. VCCs require brake throttling valves to operate in more than two quadrants and lack energy recuperation capability under overrunning loads, indirectly amplifying energy losses. The demand for efficient hydraulic systems has become increasingly critical with the growing global energy demand, environmental considerations, and sustainable industrial practices. Therefore, designing hydraulic cylinder systems that deliver comparable performance as VCCs while removing the throttling losses is important. In response to this trend, motor-controlled hydraulic cylinders (MCCs) have emerged as a promising technology, offering a more efficient alternative to VCCs.

Figure 1 provides the general structure of an MCC. An MCC incorporates a single or multiple electric motors and hydraulic pumps, an accumulator or an open tank, several auxiliary valves, and a differential hydraulic cylinder. The hydraulic cylinder is directly connected to one or two fixed-displacement hydraulic pumps driven by electric servo motors. Therefore, the cylinder motion is controlled by the electric servo motor's angular velocity. The auxiliary valves compensate for the differential flow rate, enable load-holding functionality according to different MCC architectures, or avoid cavitation. MCCs can be classified into four groups based on the number of electric servo motors and fixed-displacement hydraulic pumps utilized: one-motor-one-pump (1M1P), one-motor-two-pumps (1M2P), one-motor-three-pumps (1M3P), and two-motors-two-pumps (2M2P) MCCs [4].

Preprints.org (www.preprints.org) | NOT PEER-REVIEWED | Posted: 11 April 2024 doi:10.20944/preprints202404.0809.v1

In contrast to VCCs, the absence of valve throttling in an MCC greatly improves the system's energy efficiency. For example, a single-boom crane driven by a 1M1P MCC has been shown to consume 62 % less energy than one driven by a VCC [5]. A study of implementing six 1M1P MCCs on an excavator was conducted, as described in [6]. Experimental results demonstrated that the MCCs consumed 47.8 % less energy than the valve-controlled counterparts in a given working cycle. Furthermore, an excavator powered by three 1M2P MCCs has been shown to achieve a system efficiency of 73.3 % in a given working cycle in simulations [7]. This efficiency is significantly higher than the same excavator driven by three VCCs.

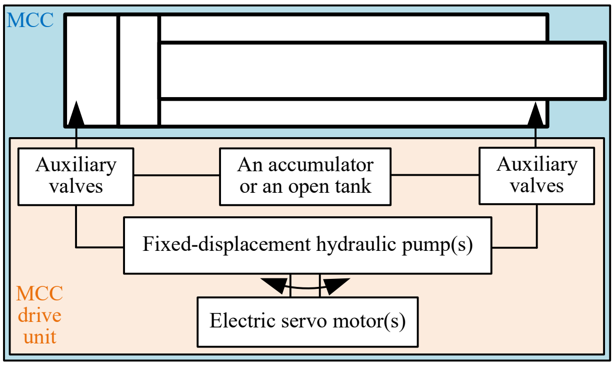

Figure 1. Structure of a motor-controlled cylinder (MCC).

It was found that a single-boom crane driven by a 1M1P MCC achieved a 75 % shorter settling time, 61 % less overshoot, and 66 % lower position tracking error compared to a single-boom crane driven by a VCC in a given working cycle [8]. The MCC's advantages have led to increased interest in MCCs from the industry. Several commercial MCC products have become available in recent years, for example, from Parker Hannifin [9], Bosch Rexroth [10], and Thomson [11].

It is worth noting that most research and commercial products related to MCCs primarily focus on the compact installation approach [12]. In this approach, all components are mounted as an integrated unit, as depicted in Figure 2. This integrated design offers advantages in terms of saving total occupied space and simplified installation. However, it has been identified that MCCs in the compact installation approach may not be suitable for large-scale knuckle boom cranes for various reasons [12]. In such cases, MCCs utilizing a remote installation approach become necessary, where the MCC drive unit shown in Figure 1 is remotely installed in the crane hydraulic machine room and connected to the cylinder with pipelines [12].

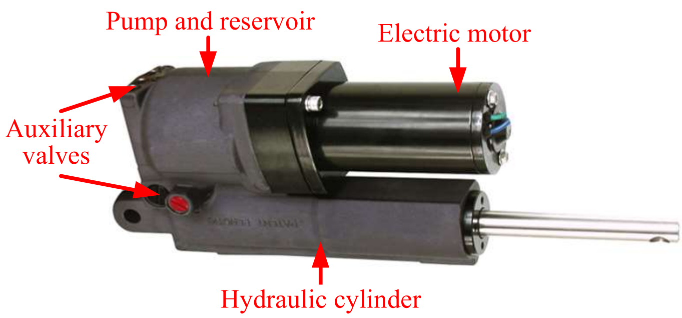

Figure 2. One-motor-one-pump (1M1P) MCC in compact installation [9].

Nevertheless, achieving a passive load-holding function in MCCs with the remote installation approach is challenging. The load-holding function in four-quadrant operation is enforced by legislation when a cylinder is used in lifting applications characterized by overrunning external load, such as cranes, trailer lifts, and scissors tables. Additionally, activating the load-holding function during standstill command is essential for energy saving and precise position control. Counterbalance valves,

Preprints.org (www.preprints.org) | NOT PEER-REVIEWED | Posted: 11 April 2024 doi:10.20944/preprints202404.0809.v1

a well-established and proven technology commonly employed in VCCs, can provide load-holding functions in MCCs in general, and in particular, during loss of power supply or hose rupture. [13,14]. However, including counterbalance valves in an MCC can decrease the system's efficiency due to the throttling losses of counterbalance valves, particularly when the load is very low. Moreover, an MCC incorporating counterbalance valves cannot realize four-quadrant operations and energy regeneration because the pilot pressure are too low to open the counterbalance valves in the second and fourth quadrants.

Besides counterbalance valves, two on/off electric valves can be used in MCCs for an active load-holding function without introducing any throttling losses [7,15]. While the normal-closed on/off electric valves can offer a load-holding function during loss of power supply, implementing load-holding functions during hose ruptures can pose challenges in a remotely installed MCC. A novel load-holding strategy for a 1M1P MCC was presented in [16]. It incorporates two pilot-operated check valves (POCVs) as load-holding valves. An electric valve connects the pilot line to the cylinder load pressures. This configuration enables the load-holding valves to be opened by hydraulic pressures instead of electric signals. Nevertheless, similar to the concept of using two on/off electric valves, this strategy lacks the capability to provide load-holding functionality in the event of hose ruptures or sudden line pressure drops.

A 2M2P MCC with a fully passive hydraulically driven load-holding device is introduced in [17]. In that study, a secondary electric servo motor and a secondary hydraulic pump are incorporated into a 1M1P MCC to manage the differential flow rate and control the minimum cylinder pressure. The load-holding valves are opened by controlling the minimum cylinder pressure over a certain level. This setup provides the desired fully hydraulically driven load-holding function, handling hose ruptures or sudden line pressure drops. However, it is important to note that the 2M2P MCC is less suitable for four-quadrant operation because the secondary servo motor and hydraulic pump cannot contribute to the cylinder's output power in quadrants II and III [18]. Therefore, a 1M1P MCC with a fully hydraulically driven passive load-holding function best fits the four-quadrant operation. Nevertheless, further research in this area is currently lacking.

This paper proposes a new 1M1P MCC design that offers a hydraulically driven passive load-holding function to address the gap mentioned above. The proposed design's functionalities are comprehensively analyzed and validated through simulations.

2. Proposed System

2.1. System Architecture

The proposed 1M1P MCC is shown in Figure 3. The system consists of two primary parts: the 1M1P MCC drive unit and the cylinder with passive load-holding devices. These two parts can be either physically integrated or positioned in separate locations connected by pipelines.

The 1M1P MCC drive unit, framed by purple dashed lines, comprises a fixed displacement pump/motor unit (P) connected to an electric servo motor/generator unit (M). A low-pressure accumulator (ACC) is used as the pressurized reservoir to supply or store the differential volume between the cylinder rod and bore sides through two pilot-operated check valves $POCV_a$ and $POCV_b$. The pilot pressures for $POCV_a$ and $POCV_b$ are line pressures p_{la} and p_{lb}, respectively. ACC maintains the minimum pump/motor unit pressure through check valves CV_7 and CV_8 to prevent cavitation. The leakage line of P is also connected to ACC via check valve CV_9. The ACC pressure p_{acc} is less than 3 bar during operations. Four 2/2 proportional solenoid valves, PSV_1 to PSV_4, are installed symmetrically around $POCV_a$ and $POCV_b$ to control the cylinder bore-side pressure p_a, cylinder rod-side pressure p_b, pump/motor unit pressure on the cylinder bore side p_{pa}, and pump/motor unit pressure on the cylinder rod side p_{pb} by throttling flows in one specific direction. Four check valves CV_3 to CV_6 are installed parallel to the PSVs to ensure free flow in the other direction. The pressure control principle is explained in detail in Section 2.2.

Preprints.org (www.preprints.org) | NOT PEER-REVIEWED | Posted: 11 April 2024 doi:10.20944/preprints202404.0809.v1

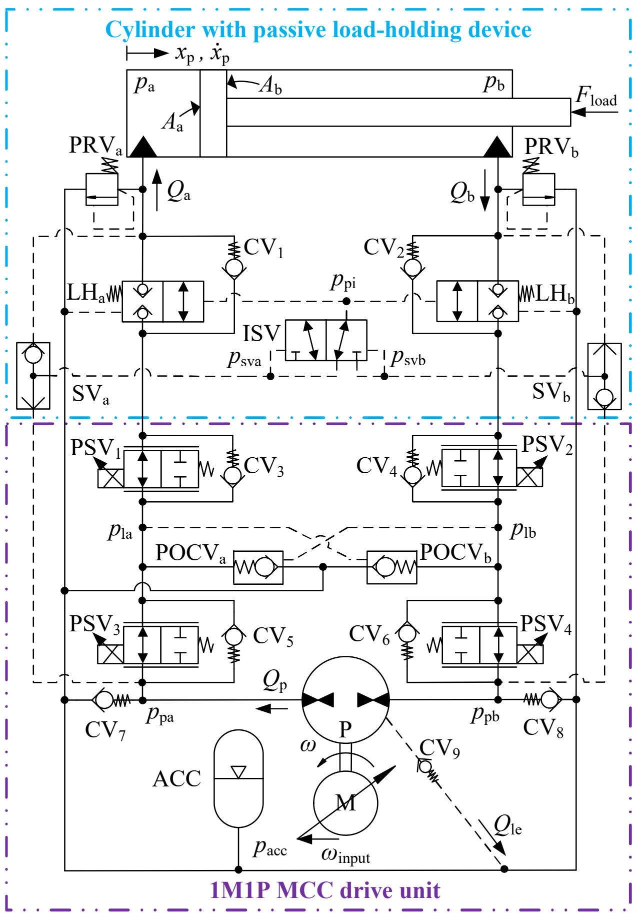

Figure 3. System architecture of the proposed 1M1P MCC.

The cylinder with passive load-holding devices is framed by light blue dashed lines. Two pressure relief valves, PRV$_a$ and PRV$_b$, are installed to limit the maximum cylinder pressures. Two 2/2 normally closed load-holding valves, LH$_a$ and LH$_b$, are opened by the pilot pressure p_{pi} when it is higher than the cracking pressure $p_{lh} = 10$ bar. Two check valves, CV$_1$ and CV$_2$, are installed in parallel to LH$_a$ and LH$_b$ to ensure free flow to the cylinder. p_{pi} is chosen as the minimum pressure between p_{sva} and p_{svb} by the inverse shuttle valve (ISV). p_{sva} and p_{svb} are the output pressures of two shuttle valves SV$_a$ and SV$_b$. p_{sva} equals the maximum pressure between p_a and p_{pa}. p_{svb} equals the maximum pressure between p_b and p_{pb}.

2.2. System Analysis in Operation Mode

In operation mode, the system can be operated in four quadrants, Q$_{I}$ to Q$_{IV}$, see Figure 4. In Q$_{I}$, the bore side pressure, p_a is the highest pressure (represented in red) in the system. M works as an electric servo motor. P works as a hydraulic pump, pumping the oil from the cylinder rod side and ACC to the cylinder bore side. LH$_a$, LH$_b$, PSV$_1$, PSV$_3$, and PSV$_4$ are fully opened. Therefore, p_a, p_{la}, p_{pa}, and p_{sva} are equal. p_{la} is higher than p_{lb} causing the opening of POCV$_b$. The accumulator flow rate Q_{acc} joins the flow from the cylinder rod side and, thereby, goes to the P inlet port, to compensate for the differential volume resulting in $p_{pb} = p_{lb} = p_{acc} = 3$ bar (represented in green). PSV$_2$ is used as an active control element throttling the flow so that p_b remains above the load holding valve crack pressure, $p_{lh} = 10$ bar. Because of the selective functions of ISV and SV$_b$, p_{pi} is equal to p_b. Thus, LH$_a$ and LH$_b$ are open.

In Q$_{II}$, the external load is assistive, and, potentially, overrunning. The rod side pressure, p_b, is the highest pressure (represented in red) in the system. M works as an electric generator. P works as a hydraulic motor, motoring the oil from the rod side to the bore side. LH$_a$, LH$_b$, PSV$_1$, PSV$_2$, and PSV$_4$

 doi:10.20944/preprints202404.0809.v1

are fully opened. Therefore, p_b, p_{lb}, p_{pb}, and p_{svb} are equal. p_{lb} is higher than p_{la} causing the opening of POCV$_a$. The accumulator flow rate Q_{acc} joins the return flow from P, and is thereby directed towards the piston side of the cylinder to compensate for the differential volume resulting in $p_a = p_{la} = p_{acc}$ (represented in green). PSV$_3$ is used as an active control element throttling the flow so that p_{pa} remains above the load holding valve crack pressure, p_{lh}. Because of the selective functions of ISV and SV$_a$, p_{pi} is equal to p_{pa}. Thus, LH$_a$ and LH$_b$ are open.

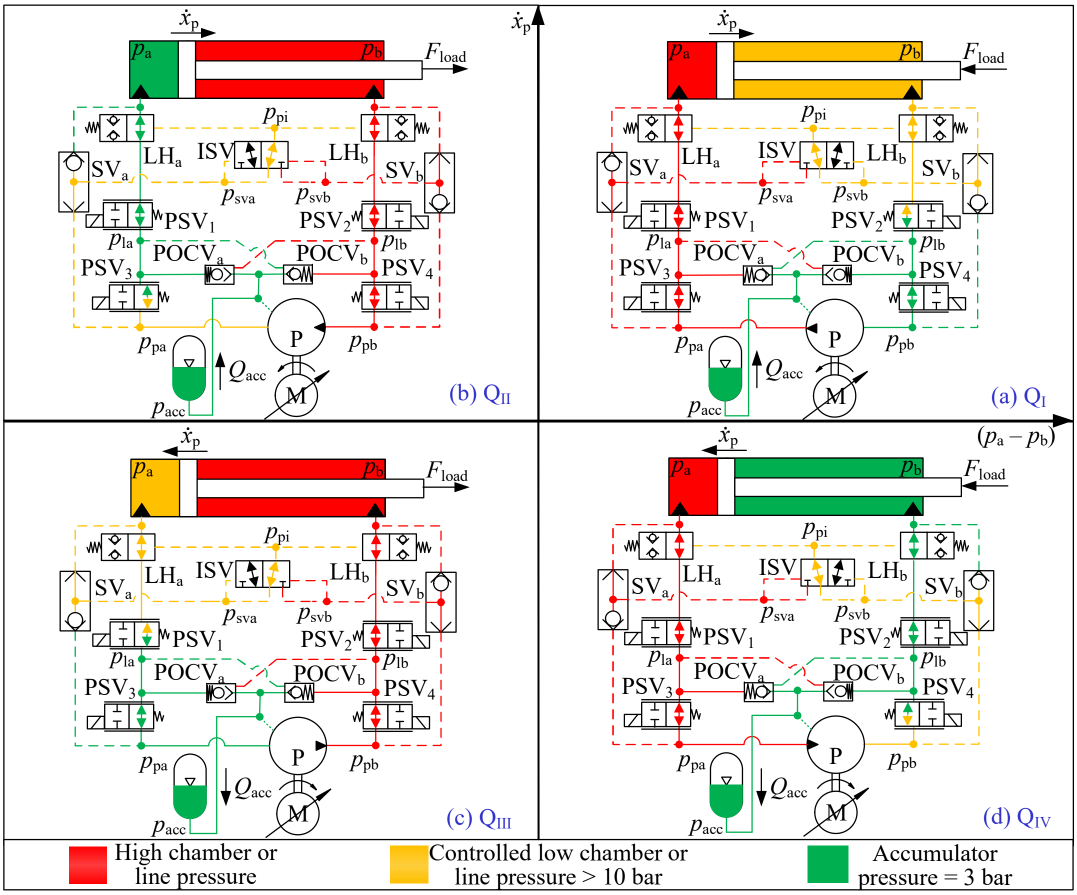

Figure 4. Demonstration of four-quadrant operations in Q_I, Q_{II}, Q_{III}, and Q_{IV}.

In Q_{III}, p_b is the highest pressure (represented in red) in the system. M works as an electric servo motor. P works as a hydraulic pump, pumping oil from the bore side to the rod side. LH$_a$, LH$_b$, PSV$_2$, PSV$_3$, and PSV$_4$ are fully opened. Therefore, p_b, p_{lb}, p_{pb}, and p_{svb} are equal. p_{lb} is higher than p_{la} causing the opening of POCV$_a$. The flow rate from the bore side is too high to be the P inlet flow rate. The differential flow rate goes back to the accumulator (Q_{acc}) resulting in $p_{la} = p_{pa} = p_{acc}$ (represented in green). PSV$_1$ is used as an active control element throttling the flow so that p_a remains above the load holding valve crack pressure, p_{lh}. Because of the selective functions of ISV and SV$_a$, p_{pi} is equal to p_a. Thus, LH$_a$ and LH$_b$ are open.

In Q_{IV}, the external load is assistive, and, potentially, overrunning. The bore side pressure, p_a is the highest pressure (represented in red) in the system. M works as an electric generator. P works as a hydraulic motor, motoring oil from the bore side to the rod side. LH$_a$, LH$_b$, PSV$_1$, PSV$_2$, and PSV$_3$ are fully opened. Therefore, p_a, p_{la}, p_{pa}, and p_{sva} are equal. p_{la} is higher than p_{lb} causing the opening of POCV$_b$. The flow rate from the bore side passing through the p is too high for the rod side. The differential flow rate goes back to the accumulator (Q_{acc}) resulting in resulting in $p_b = p_{la} = p_{acc}$ (represented in green). PSV$_4$ is used as an active control element throttling the flow so that p_{pb} remains above the load holding valve crack pressure, p_{lh}. Because of the selective functions of ISV and SV$_b$, p_{pi} is equal to p_{pb}. Thus, LH$_a$ and LH$_b$ are open.

 doi:10.20944/preprints202404.0809.v1

2.3. System Analysis in Load-Holding Mode

For all four quadrants, the load holding can be introduced quite simply by opening the active control elements fully. In that case p_{pi} will always go below the p_{lh} value and the load holding valves will close. This is illustrated in Figure 5.

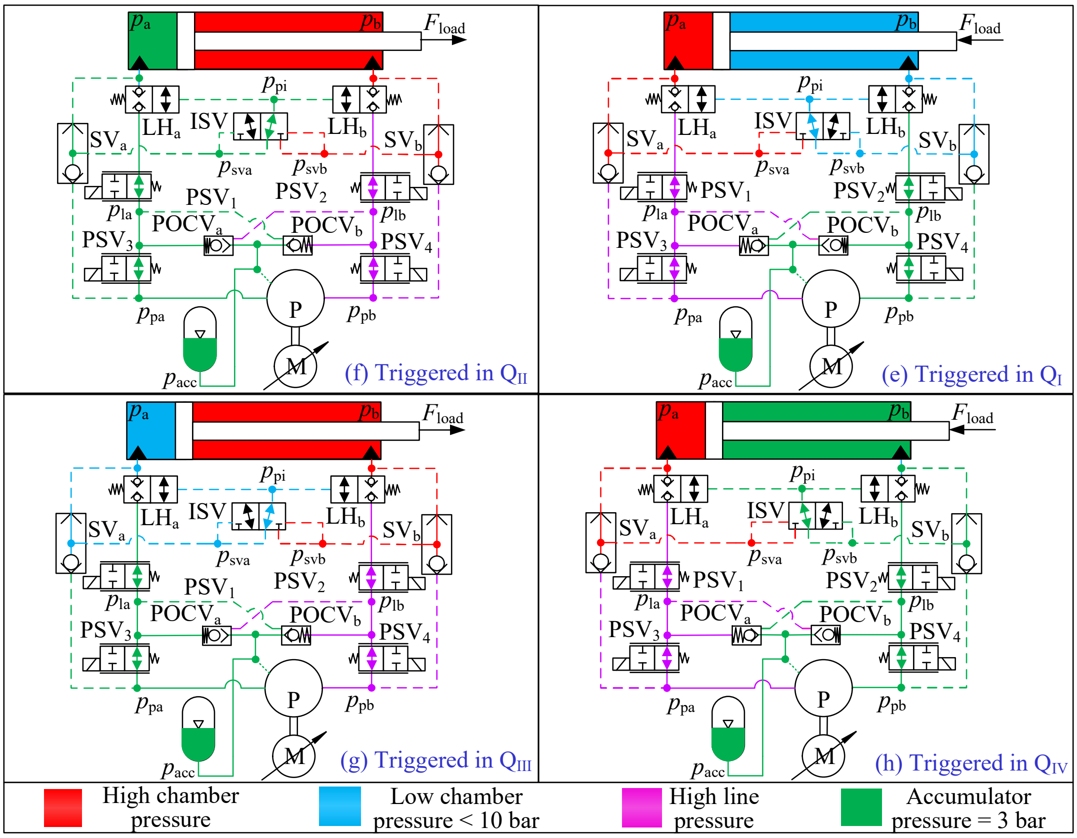

Figure 5. Demonstration of load-holding mode triggered in four-quadrant operation.

3. System Modeling

The dynamic system model of the proposed 1M1P MCC is derived based on the experimentally validated system model of a 2M2P MCC utilized in [18]. The selected off-the-shelf components of the proposed 1M1P MCC are listed in Table 1. The modeling parameters are from the datasheet of these components.

Table 1. Off-the-shelf components of the proposed 1M1P MCC in Figure 3.

Components	Manufacturer	Product number
M	Bosch Rexroth	MS2N07-D
P	Bosch Rexroth	A10FZG
ACC	Bosch Rexroth	HAD3,5-250-2X
ISV	Bucher	HOSV-10
LH	Sun Hydraulics	DKHSXHN
CV	Bosch Rexroth	RE20380
PRV	Bosch Rexroth	RE 25402
PSV	Bosch Rexroth	KKDSR1PB
POCV	Sun Hydraulics	CKEBXCN
SV	Bosch Rexroth	MHSU2KA1X/420
Cylinder	LJM	NH41-0-SD

M is modeled by a second-order transfer function, see Equation 1. In this equation, ω_{input} denotes the input signal to the motor from the position controller, and ω represents the resulting motor shaft

 doi:10.20944/preprints202404.0809.v1

velocity. The motor dynamics are characterized by a natural frequency ω_n of 23.8 Hz and a damping ratio ζ of 0.73. According to the datasheet, the energy efficiency (η_M) of M is 95 %. For the purposes of this paper, saturation limits for M are not reached and are thus disregarded.

$$\frac{\omega}{\omega_\mathrm{input}} = \frac{\omega_\mathrm{n}^2}{s^2 + 2\omega_\mathrm{n}\zeta s + \omega_\mathrm{n}^2} \tag{1}$$

P is rigidly connected to M and rotates at the same angular velocity (ω). The pump flow rate (Q_p) is modeled using Equation 2, with a displacement of $D = 6$ cc/rev. The modeling of leakages ($Q_\mathrm{le,l}$ and $Q_\mathrm{le,r}$) in P uses Equations 3 and 4. Δp_l represents the pressure difference between the left side of the pump and the accumulator. In contrast, Δp_r represents the pressure difference between the right side of the pump and the accumulator. The pump leakage coefficient (k_le) is $2.5 \cdot 10^{-3}$ L/min/bar. Therefore, the pump flow rates on the right side (Q_pa) and left side (Q_pb) are expressed in Equation 5 and 6. Experimental data in [18] indicates that the leakage between the two sides of the cylinder is insignificant and therefore is neglected.

$$Q_\mathrm{p} = D\omega \tag{2}$$

$$Q_\mathrm{le,l} = \Delta p_\mathrm{l} k_\mathrm{le} \tag{3}$$

$$Q_\mathrm{le,r} = \Delta p_\mathrm{r} k_\mathrm{le} \tag{4}$$

$$Q_\mathrm{pa} = D\omega - Q_\mathrm{le,l} \tag{5}$$

$$Q_\mathrm{pb} = -D\omega - Q_\mathrm{le,r} \tag{6}$$

The theoretical torque (T_th) of P is derived via Equation 7. The torque loss (T_s) of P is derived by scaling a reference torque losses ($T_\mathrm{s,ref}$) from steady-state experimental data of a reference axial-piston unit with displacement equal to D_ref = 75 cc/rev [19]. $T_\mathrm{s,ref}$ is a function of ω and $p_\mathrm{pa} - p_\mathrm{pb}$. The same method is also used in [16]. The scaling factor (λ) and torque loss (T_s) are calculated via Equation 8 and 9, respectively.

$$T_\mathrm{th} = D(p_\mathrm{pa} - p_\mathrm{pb}) \tag{7}$$

$$\lambda = \sqrt[3]{\frac{D}{D_\mathrm{ref}}} \tag{8}$$

$$T_\mathrm{s} = \lambda^3 T_\mathrm{s,ref} \tag{9}$$

The hydraulic system is simulated using an approach where the effective bulk modulus ($\beta_{\mathrm{chb},i}$) of the fluid in the i-th hydraulic chamber is determined through a combination of Equations 10, 11, and 12. β_oil = 7000 bar is the hydraulic oil's bulk modulus. $p_{\mathrm{chb},i}$ is the pressure in i-th hydraulic chamber. p_atm = 1 bar is the atmospheric pressure. k_air = 1.4 is the air adiabatic constant. $\beta_{\mathrm{chb,air},i}$ is the i-th chamber entrapped air bulk modulus. $V_{\mathrm{atm},\varepsilon}$ = 0.01 is the entrapped air relative volume at atmospheric pressure. $V_{\mathrm{chb},\varepsilon,i}$ is the entrapped air relative volume in the i-th chamber. The Greek letter, ε, represents the volume ratio between undissolved gas and oil at atmospheric pressure.

$$\beta_{\mathrm{chb},i} = p_{\mathrm{chb},i} k_\mathrm{air} \tag{10}$$

$$V_{\mathrm{chb},\varepsilon,i} = V_{\mathrm{atm},\varepsilon} \left(\frac{p_\mathrm{atm}}{p_{\mathrm{chb},i}} \right)^{\frac{1}{k_\mathrm{air}}} \tag{11}$$

$$\beta_{\mathrm{chb},i} = \frac{1}{\frac{1}{\beta_\mathrm{oil}} + \frac{V_{\mathrm{chb},\varepsilon,i}}{\beta_{\mathrm{chb,air},i}}} \tag{12}$$

 doi:10.20944/preprints202404.0809.v1

The hydraulic cylinder model comprises three parts: pressure build-up, pressure-force conversion, and cylinder friction. The pressure build-up on the bore side ($\dot{p}_{\mathrm{a}}$) and rod side ($\dot{p}_{\mathrm{b}}$) of the cylinder are represented by Equations 13 and 14. The flow rates going in or out of the cylinder bore and rod sides are denoted by Q_{a} and Q_{b}. The piston position and velocity are represented by x_{p} and $\dot{x}_{\mathrm{p}}$, respectively. The bore and rod side areas are denoted by A_{a} and A_{b}, respectively. The maximum cylinder stroke is $x_{\mathrm{end}} = 400$ mm, with a bore side diameter of 63 mm and a rod side diameter of 45 mm. The cylinder dead volume plus line volume is denoted by V_0. The pressure-force conversion (F_{cyl}) is modeled via Equation 15. The frictional interaction between the cylinder and piston is modelled as Stribeck friction, see Equation 16. The viscous friction coefficient is denoted as f_{v} and is equal to 4000 Ns/m. The coulomb friction force is represented by F_{C} and is equal to 75 N. The hyperbolic tangent coefficient is γ, which is equal to 250 s/m. The static friction force is F_{S}, with a value of 500 N. The static friction time constant is τ, with a value of 0.02 m/s. It should be noted that the complexity of cylinder friction can vary, and incorporating factors like the pressure difference ($p_{\mathrm{a}} - p_{\mathrm{b}}$) may provide a more detailed representation. However, in this study, the pressure levels are similar across experiments. Therefore, the Stribeck friction model is considered adequate.

$$\dot{p}_{\mathrm{a}} = \frac{\beta_{\mathrm{chb,a}}(Q_{\mathrm{a}} - \dot{x}_{\mathrm{p}} A_{\mathrm{a}})}{V_0 + x_{\mathrm{p}} A_{\mathrm{a}}} \tag{13}$$

$$\dot{p}_{\mathrm{b}} = \frac{\beta_{\mathrm{chb,b}}(\dot{x}_{\mathrm{p}} A_{\mathrm{b}} - Q_{\mathrm{b}})}{V_0 + (x_{\mathrm{end}} - x_{\mathrm{p}}) A_{\mathrm{b}}} \tag{14}$$

$$F_{\mathrm{cyl}} = p_{\mathrm{a}} A_{\mathrm{a}} - p_{\mathrm{b}} A_{\mathrm{b}} \tag{15}$$

$$F_{\mathrm{f}} = f_{\mathrm{v}} \dot{x}_{\mathrm{p}} + \tanh(\gamma \dot{x}_{\mathrm{p}}) \left(F_{\mathrm{C}} + F_{\mathrm{S}} \mathrm{e}^{\frac{-\dot{x}_{\mathrm{p}} \tanh(\gamma \dot{x}_{\mathrm{p}})}{\tau}} \right) \tag{16}$$

The modeling approach for the bladder accumulator follows the method proposed in [20]. According to Equation 17, the gas pressure (p_{g}) is equivalent to the fluid pressure (p_{f}) when the fluid pressure is greater than the pre-charged gas pressure ($p_{\mathrm{g0}} = 0.96$ bar), which in this paper is considered to be always true. When the gas pressure changes, the gas volume (V_{g}) is modeled via Eq. 18. The symbol n represents the adiabatic gas constant. The fluid volume (V_{f}) is calculated as the difference in total accumulator volume ($V_{\mathrm{g0}} = 2.8$ L) and gas volume (V_{g}), as shown in Equation 19. The fluid pressure build-up ($\dot{p}_{\mathrm{f}}$) is modeled via Equation 20. The fluid volume changing rate ($\dot{V}_{\mathrm{f}}$) is calculated via Equation 21. The accumulator pressure (p_{acc}) is equal to the fluid pressure (p_{f}).

$$p_{\mathrm{g}} = \begin{cases} p_{\mathrm{f}} & \text{if } p_{\mathrm{g}} \geq p_{\mathrm{g0}} \\ p_{\mathrm{g0}} & \text{if } p_{\mathrm{f}} < p_{\mathrm{g0}} \end{cases} \tag{17}$$

$$V_{\mathrm{g}} = \left(\frac{p_{\mathrm{g0}} V_{\mathrm{g0}}^{n}}{p_{\mathrm{g}}} \right)^{\frac{1}{n}} \tag{18}$$

$$V_{\mathrm{f}} = V_{\mathrm{g0}} - V_{\mathrm{g}} \tag{19}$$

$$\dot{p}_{\mathrm{f}} = \frac{\beta_{\mathrm{chb,acc}}}{V_{\mathrm{f}}} (Q_{\mathrm{acc}} - \dot{V}_{\mathrm{f}}) \tag{20}$$

$$\dot{V}_{\mathrm{f}} = -\dot{V}_{\mathrm{g}} = \left(\frac{1}{1 + \frac{n p_{\mathrm{f}} V_{\mathrm{f}}}{\beta_{\mathrm{chb,acc}} V_{\mathrm{g}}}} \right) Q_{\mathrm{acc}} \tag{21}$$

Preprints.org (www.preprints.org) | NOT PEER-REVIEWED | Posted: 11 April 2024 doi:10.20944/preprints202404.0809.v1

Nine CVs are used in the proposed 1M1P MCC, as shown in Figure 3. Equation 22 is used to model the behavior of all these CVs. $\Delta p_{\text{cv,i}}$ represents the pressure drop across the i-th CV, and $Q_{\text{cv,i}}$ denotes the corresponding flow rate. The same cracking pressure $p_{\text{cv,cr}} = 0.2$ bar is used for all CVs, and they all have the same CV flow rate constant of $k_{\text{cv}} = 500$ L/min/bar.

$$Q_{\text{cv,i}} = \begin{cases} 0 & \text{if } (\Delta p_{\text{cv},i} - p_{\text{cv,cr}}) \leq 0 \\ (\Delta p_{\text{cv},i} - p_{\text{cv,cr}})k_{\text{cv}} & \text{if } (\Delta p_{\text{cv},i} - p_{\text{cv,cr}}) > 0 \end{cases} \tag{22}$$

Two SVs and an ISV are used in the pilot lines. They are modeled as logic elements. Equation 23 shows the logic of ISV. Equation 24 and 25 show the logic of SV_{a} and SV_{b}, respectively.

$$p_{\text{pi}} = \begin{cases} p_{\text{sva}} & \text{if } p_{\text{sva}} \leq p_{\text{svb}} \\ p_{\text{svb}} & \text{if } p_{\text{sva}} > p_{\text{svb}} \end{cases} \tag{23}$$

$$p_{\text{sva}} = \begin{cases} p_{\text{pa}} & \text{if } p_{\text{a}} \leq p_{\text{pa}} \\ p_{\text{a}} & \text{if } p_{\text{a}} > p_{\text{pa}} \end{cases} \tag{24}$$

$$p_{\text{svb}} = \begin{cases} p_{\text{pb}} & \text{if } p_{\text{b}} \leq p_{\text{pb}} \\ p_{\text{b}} & \text{if } p_{\text{b}} > p_{\text{pb}} \end{cases} \tag{25}$$

The modeling approach for the two non-vented pressure-operated check valves (POCVs) aligns with the method presented in [16]. The calculation of the flow rates through POCVs, denoted as $Q_{\text{POCV},i}$, is performed using the orifice equation shown in Equation 26.

$$Q_{\text{POCV},i} = \begin{cases} 0 & \text{if } p_{\text{out},i} > p_{\text{in},i} + \psi p_{\text{x},i} \\ K_{\text{pocv},i} u_i \text{SIGN}(\Delta p_i) \sqrt{\frac{2}{\rho}|\Delta p_i|} & \text{if } p_{\text{out},i} \leq p_{\text{in},i} + \psi p_{\text{x},i} \end{cases} \tag{26}$$

This equation takes the following properties into account: a pressure differential across the valve (Δp_i), a valve opening constant ($K_{\text{pocv},i}$), a dimensionless poppet lift (u_i), a pilot ratio (ψ), fluid density (ρ), a valve inlet pressure ($p_{\text{in},i}$), and a valve outlet pressure ($p_{\text{out},i}$). The symbol, i, represents the i-th POCV. The dimensionless poppet lift, u_i, is computed in two different ways depending on the mode of operation. If the POCV is acting as a regular check valve it is computed via Equation 27, and if it is acting as a pilot operated check valve it is computed via Equation 28.

$$u_i = \frac{p_{\text{in},i} - p_{\text{out},i} - p_{\text{pocv,cr}}}{\Delta p_{\text{open}}} \tag{27}$$

$$u_i = \frac{\psi(p_{\text{x},i} - p_{\text{in},i}) + (p_{\text{in},i} - p_{\text{out},i}) - p_{\text{pocv,cr}}}{\Delta p_{\text{open}}} \tag{28}$$

In the equations, $p_{\text{x},i}$ represents the pilot pressure, $p_{\text{pocv,cr}}$ represents the valve cracking pressure, and Δp_{open} represents the pressure difference required to fully open the check valve.

The modelling approach of four PSVs is similar as for the POCVs, i.e. Equation 29. The symbol $K_{\text{psv},i}$ is the opening area constant for the i-th PSV. The symbol $\Delta p_{\text{psv},i}$ is the pressure differential across the i-th PSV. The dimensionless opening for each PSV, $u_{\text{psv},i}$, is given by the control signal to the solenoid. Finally, the modelling approach for two load-holding valves follows a similar orifice equation with the dimensionless opening defined from the pilot pressure p_{pi} and the valve crack pressure.

$$Q_{\text{psv},i} = K_{\text{psv},i} u_{\text{psv},i} \text{SIGN}(\Delta p_{\text{psv},i}) \sqrt{\frac{2}{\rho}|\Delta p_{\text{psv},i}|} \tag{29}$$

Preprints.org (www.preprints.org) | NOT PEER-REVIEWED | Posted: 11 April 2024 doi:10.20944/preprints202404.0809.v1

p_{la}, p_{lb}, p_{pa}, and p_{pb} are calculated by the pressure build-up equations, as shown in Equations 30 to 33. V_{la}, V_{lb}, V_{pa}, and V_{pb} are the volumes of the transmission lines. Because of CV_3 (or CV_4) when the hose between LH_a (or LH_b) and PSV_1 (or PSV_2) ruptures, p_{la} (or p_{lb}) becomes zero. Therefore, the hose rupture is realized by forcing p_{la} (or p_{lb}) to zero at 60 s in simulations.

$$\dot{p}_{\text{la}} = \frac{\beta_{\text{chb,la}}(Q_{\text{pocv},a} + Q_{\text{psv,3}} - Q_{\text{psv,1}})}{V_{\text{la}}} \tag{30}$$

$$\dot{p}_{\text{lb}} = \frac{\beta_{\text{chb,lb}}(Q_{\text{pocv},b} + Q_{\text{psv,4}} - Q_{\text{psv,2}})}{V_{\text{lb}}} \tag{31}$$

$$\dot{p}_{\text{pa}} = \frac{\beta_{\text{chb,pa}}(Q_{\text{pa}} - Q_{\text{psv,3}})}{V_{\text{pa}}} \tag{32}$$

$$\dot{p}_{\text{pb}} = \frac{\beta_{\text{chb,pb}}(Q_{\text{pb}} - Q_{\text{psv,4}})}{V_{\text{pb}}} \tag{33}$$

The laboratory single-boom crane investigated in a previous experiment study [18] is used in this paper as an application to verify the proposed 1M1P MCC's functionalities. This crane is modeled in the Simulink-Simscape. The crane model receives the hydraulic cylinder force from the hydraulic system model and provides piston position and velocity back to the hydraulic system model. The crane is shown in Figure 6 with some of the main inertia data. The total mass of the crane boom and the payload is 300.8 kg, with the mass center located at a distance of 1.77 m from the hinge.

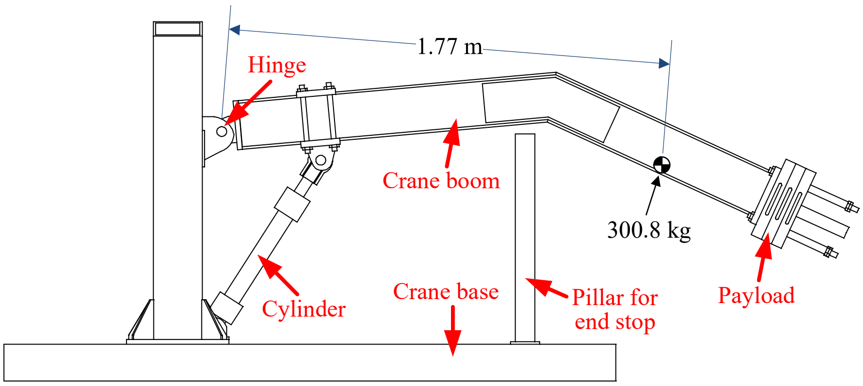

Figure 6. Sketch of the laboratory single-boom crane.

4. Controls

The control algorithm for the proposed 1M1P MCC is presented in this section. Figure 7 illustrates the control algorithm, which incorporates three distinct control loops: the position control loop, the line pressure control loop, and the PSV control loop. These control loops enable the MCC to operate in either the operation mode or the load-holding mode, depending on the specific working conditions.

 doi:10.20944/preprints202404.0809.v1

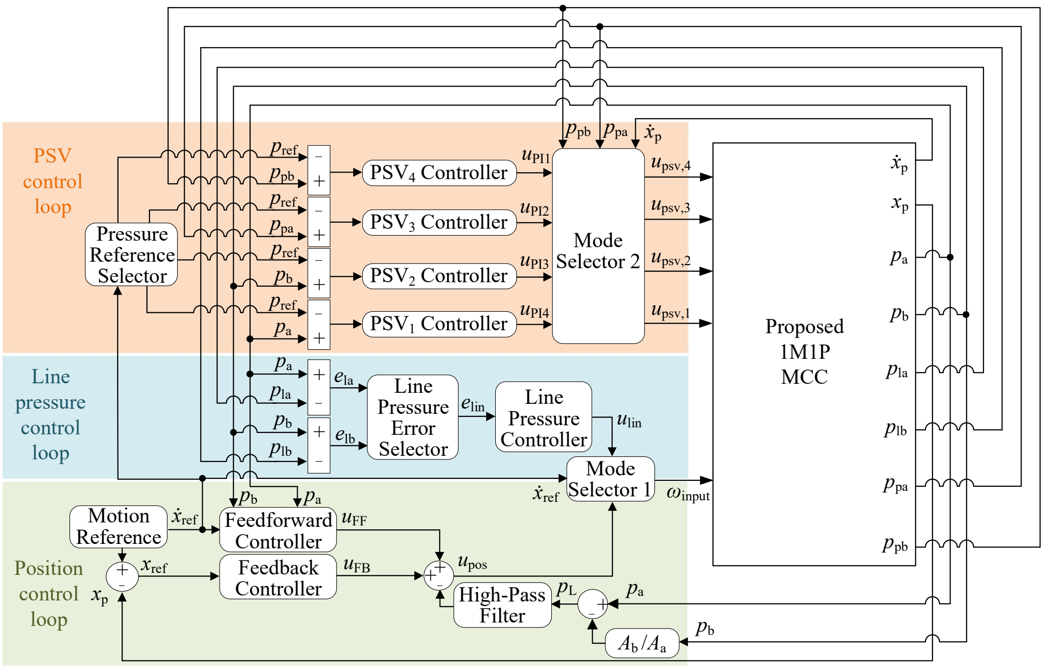

Figure 7. Block diagram of the control algorithm.

4.1. Position Control Loop

The green area in Figure 7 shows the position control loop. It is activated via the block Mode Selector 1 in the operation mode. Mode Selector 1 works based on the speed reference $\dot{x}_{\mathrm{ref}}$, as illustrated in Equation 34. ω_{input} is the input command to M. u_{pos} is the position control loop output. u_{lin} is the line pressure control loop output.

$$\omega_{\mathrm{input}} = \begin{cases} u_{\mathrm{pos}} & \text{if } \dot{x}_{\mathrm{ref}} \neq 0 \ \ \text{(operation mode)} \\ u_{\mathrm{lin}} & \text{if } \dot{x}_{\mathrm{ref}} = 0 \ \ \text{(load-holding mode)} \end{cases} \tag{34}$$

The position control loop comprises three terms, feedforward, feedback, and a high pass filtered pressured feedback. The feedforward controller estimates the required speed of M (u_{FF}) via Equation 35. The cylinder bore-side area A_{a}, the cylinder rod-side area A_{b}, and the displacement D of P are recalled. A proportional-integral controller yields the necessary feedback controller command (u_{FB}) to correct the feedforward prediction. The proportional gain is $5.85{\cdot}10^5$ rev/min/m, and the integral gain is $1.05{\cdot}10^5$ rev/min/m/s.

$$u_{\mathrm{FF}} = \begin{cases} \frac{\dot{x}_{\mathrm{ref}} A_{\mathrm{a}}}{D} & \text{if } p_{\mathrm{a}} \geq p_{\mathrm{b}} \ \ (Q_{\mathrm{I}} \text{ and } Q_{\mathrm{IV}}) \\ \frac{\dot{x}_{\mathrm{ref}} A_{\mathrm{b}}}{D} & \text{if } p_{\mathrm{a}} < p_{\mathrm{b}} \ \ (Q_{\mathrm{II}} \text{ and } Q_{\mathrm{III}}) \end{cases} \tag{35}$$

A load-pressure feedback signal (p_{L}) calculated via the bore-side pressure (p_{a}), the rod-side pressure (p_{b}), and the area ratio ($A_{\mathrm{b}}/A_{\mathrm{a}}$) is filtered by a high-pass filter (G_{HP}) shown in Equation 36. The cut-off frequency (ω_{HP}) is 3 rad/s. The filter gain (k_{HP}) is 5 rev/min/bar. The negative filtered load-pressure feedback signal is added to increase the system damping.

$$G_{\mathrm{HP}} = k_{\mathrm{HP}} \frac{s}{s + \omega_{\mathrm{HP}}} \tag{36}$$

4.2. Line Pressure Control Loop

The blue area in Figure 7 represents the line pressure control loop. The primary objective of this control loop is to minimize the pressure deviation between the cylinder pressure (p_{a} or p_{b}) and the

Preprints.org (www.preprints.org) | NOT PEER-REVIEWED | Posted: 11 April 2024 doi:10.20944/preprints202404.0809.v1

line pressure (p_{la} or p_{lb}) in load-holding mode. By doing so, the piston oscillation that occurs during the transition between the operation and load-holding modes can be effectively mitigated.

Only the line pressure on the load-holding side, i.e., p_{la} in Q_{I} and Q_{IV} or p_{lb} in Q_{II} and Q_{III}, is controlled in this loop. This is realized by the line pressure error selector block represented via Equation 37. e_{lin} is the line pressure error to the controller. $e_{\mathrm{la}} = p_{\mathrm{a}} - p_{\mathrm{la}}$ is the line pressure error on the cylinder bore side. $e_{\mathrm{lb}} = p_{\mathrm{b}} - p_{\mathrm{lb}}$ is the line pressure error on the cylinder rod side. $p_{\mathrm{o}} = 2$ bar is a pressure offset to ensure the line pressure is lower than the cylinder pressure. This offset is essential to prevent the control loop from causing control overshoot, which could raise the line pressures above the cylinder pressures before opening the load-holding valves. In that case, the cylinder begins moving before the load-holding valves are fully open.

$$e_{\mathrm{lin}} = \begin{cases} e_{\mathrm{la}} - p_{\mathrm{o}} & \text{if } p_{\mathrm{a}} \geq p_{\mathrm{b}} \ \ (Q_{\mathrm{I}} \ \text{ and } \ Q_{\mathrm{IV}}) \\ e_{\mathrm{lb}} - p_{\mathrm{o}} & \text{if } p_{\mathrm{a}} < p_{\mathrm{b}} \ \ (Q_{\mathrm{II}} \ \text{ and } \ Q_{\mathrm{III}}) \end{cases} \tag{37}$$

The line pressure controller, a proportional-integral controller, generates the command u_{lin} to the mode selector 1. The proportional gain is 24 rev/bar, and the integral gain is 12 rev/bar/s.

4.3. PSV Control Loop

The orange area in Figure 7 shows the PSV control loop. As analyzed in Section 2, the system incorporates four normally open PSVs to regulate the pressures (p_{a}, p_{b}, p_{pa}, and p_{pb}), which operate the load-holding device and mitigate the pump mode oscillation. These PSVs are individually controlled by identical feedback proportional-integral controllers. The proportional gain is 1 bar^{-1}, and the integral gain is 0.01 s/bar. It should be noted that the control errors are generated using the feedback pressures minus the reference pressures. In this way, PSVs are opened by the controllers if the reference pressure is higher than the feedback pressure and closed if the reference pressure is lower than the feedback pressure. The pressure reference (p_{ref}) is the same for all controllers. The pressure reference selector generates two different pressure references according to different modes, as expressed in Equation 38. Because the ACC pressure (p_{acc}) is 3 bar, PSVs are fully opened in the load-holding mode. Higher pressure reference in operation mode increases the PSV energy losses. Thus, a low pressure reference is preferred. However, it cannot be lower than 10 bar, which is the cracking pressure of the load-holding valves. Hence, 15 bar is chosen as the pressure reference in the operation mode, considering a safety factor.

$$p_{\mathrm{ref}} = \begin{cases} 15 \text{ bar} & \text{if } \dot{x}_{\mathrm{ref}} \neq 0 \ \ (\text{operation mode}) \\ 3 \text{ bar} & \text{if } \dot{x}_{\mathrm{ref}} = 0 \ \ (\text{load-holding mode}) \end{cases} \tag{38}$$

In Q_{III}, PSV_1 is actively controlled, while the other PSVs are fully open. Similarly, in QI, PSV_2 is actively controlled, while the other PSVs are fully open. This pattern continues in Q_{II} and Q_{IV}, where PSV_3 and PSV_4 are actively controlled, respectively, with the remaining PSVs fully open. These control actions are implemented through the Mode Selector 2 block using Equations 39 to 42. Here, $u_{\mathrm{psv,1}}$ to $u_{\mathrm{psv,4}}$ represent PSV input commands, while u_{PI1} to u_{PI4} denote the outputs of the four PSV controllers.

$$u_{\mathrm{psv,1}} = \begin{cases} u_{\mathrm{PI1}} & \text{if } \dot{x}_{\mathrm{P}} \leq 0 \ \text{ and } (p_{\mathrm{a}} - p_{\mathrm{b}}) \leq 0 \\ 1 & \text{Other} \end{cases} \tag{39}$$

$$u_{\mathrm{psv,2}} = \begin{cases} u_{\mathrm{PI2}} & \text{if } \dot{x}_{\mathrm{P}} \geq 0 \ \text{ and } (p_{\mathrm{a}} - p_{\mathrm{b}}) \geq 0 \\ 1 & \text{Other} \end{cases} \tag{40}$$

$$u_{\mathrm{psv,3}} = \begin{cases} u_{\mathrm{PI3}} & \text{if } \dot{x}_{\mathrm{P}} \geq 0 \ \text{ and } (p_{\mathrm{a}} - p_{\mathrm{b}}) \leq 0 \\ 1 & \text{Other} \end{cases} \tag{41}$$

$$u_{\mathrm{psv},4} = \begin{cases} u_{\mathrm{PI4}} & \text{if } \dot{x}_{\mathrm{P}} \leq 0 \text{ and } (p_{\mathrm{a}} - p_{\mathrm{b}}) \geq 0 \\ 1 & \text{Other} \end{cases} \tag{42}$$

5. Simulation Results

In order to evaluate the proposed 1M1P MCC in four-quadrant operations and its load-holding functions, a representative working trajectory is used for the 1M1P MCC driving the single-boom crane in simulations. This trajectory encompasses the extension and retraction of the hydraulic cylinder across three distinct load-holding periods. The given trajectory corresponds to a piston velocity of 20 mm/s, representing a common working speed of the single-boom crane. In the result plots, LH and LH_1 indicate the load-holding modes under standstill command and hose rupture situation, while $\mathrm{Q_I}$, $\mathrm{Q_{II}}$, $\mathrm{Q_{III}}$, and $\mathrm{Q_{IV}}$ denote the system's operation in the first, second, third, and fourth quadrant, respectively. The system achieves four-quadrant operations by manipulating the direction of gravity, generating two distinct scenarios: scenario A and scenario B. In scenario A, gravity is directed downwards, allowing the system to operate in quadrants $\mathrm{Q_I}$ and $\mathrm{Q_{IV}}$, as depicted in Figure 8a. Conversely, in scenario B, gravity is directed upwards, enabling the system to operate in quadrants $\mathrm{Q_{II}}$ and $\mathrm{Q_{III}}$, as illustrated in Figure 8b.

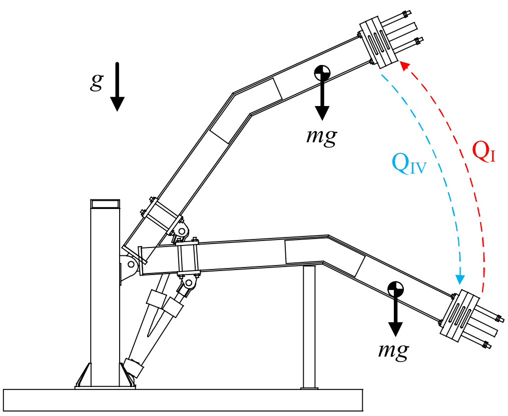

(a) Operation in $\mathrm{Q_I}$ and $\mathrm{Q_{IV}}$.

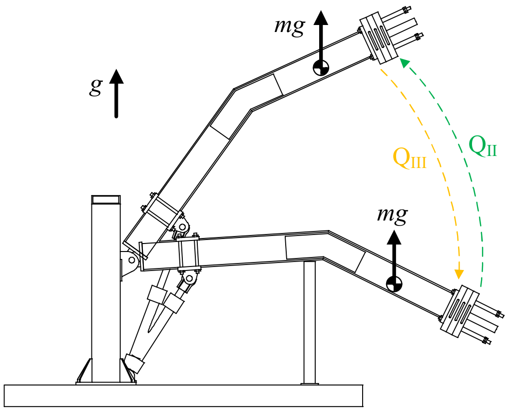

(b) Operation in $\mathrm{Q_{II}}$ and $\mathrm{Q_{III}}$.

Figure 8. Four-quadrant operations by altering the gravity direction.

5.1. Results in Scenario A

The position tracking performance in scenario A is shown in Figure 9a and 9b. The hose connecting the drive unit and the cylinder on the high pressure side ruptures at 60 s, which is realized via forcing p_{la} (or p_{lb}) to zero. The position feedback signal (FB) tracks the position reference (Ref) well. The tracking error before hose rupture falls well within ± 2 mm. The error peaks occur at transitions between load-holding and operation modes. It is important to note that the tracking error after 60 seconds is not shown in the figure, as the feedback signal cannot follow the reference due to the hose rupture situation. The stable error in LH demonstrates the load-holding function under the standstill command. It is important to emphasize that the standstill command scenario is analogous to a system power loss emergency. Therefore, the load-holding function during system power loss is also successfully verified. Furthermore, the maintained piston position in LH_1 demonstrates the load-holding function after hose rupture at 60 s.

Preprints.org (www.preprints.org) | NOT PEER-REVIEWED | Posted: 11 April 2024 doi:10.20944/preprints202404.0809.v1

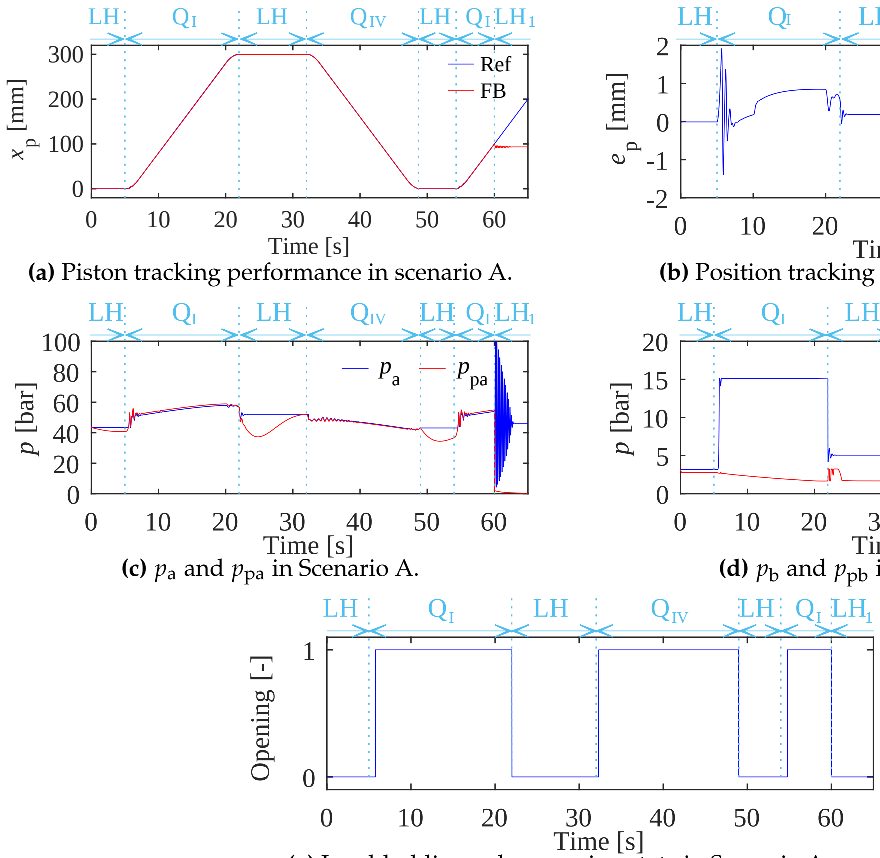

(a) Piston tracking performance in scenario A. **(b)** Position tracking error in scenario A. **(c)** p_a and p_{pa} in Scenario A. **(d)** p_b and p_{pb} in Scenario A. **(e)** Load-holding valve opening state in Scenario A.

Figure 9. Simulation results in scenario A.

System pressures in scenario A are shown in Figure 9c and 9d. p_{pa} is controlled close to p_a, demonstrating the functionality of the line pressure control loop. Furthermore, the stability observed in p_a and p_b during LH provides additional evidence of the effective load-holding function. However, at the beginning of LH_1, significant pressure oscillations in p_a and p_b occur due to the sudden hose rupture. These oscillations gradually cease after a transitional period. Because of the hose rupture, p_{pa} drops to zero promptly. Before the hose ruptures, p_b is controlled at 15 bar by PSV_2 in Q_I. p_{pb} is controlled at 15 bar by PSV_4 in Q_{IV}. These two controlled pressures are used to open the load-holding valves. Figure 9e shows the load-holding valve opening state. The load-holding valve opening state is linked to the controlled pressures p_b and p_{pb}. Notably, a delay in opening the load-holding valves is observed at the beginning of Q_I. This delay is because p_b is increased by the pump/motor unit via increasing p_a, and the commanded pump/motor unit speed is slow at the beginning of Q_I. Consequently, this delay contributes to peak errors in position tracking, as illustrated in Figure 9b. As shown in Figure 9e, the load-holding valves are closed immediately in both LH and LH_1.

5.2. Results in Scenario B

As shown in Figure 8b, the gravity in scenario B is directed to the opposite of scenario A to generate operations in Q_{II} and Q_{III}. Figure 10a and 10b show the position tracking performance in scenario B. The tracking error before the hose rupture on the high pressure side (Equation 31) falls well within ± 3 mm. Due to the delay in opening the load-holding valves, the error peaks occur at transitions between load-holding and operation modes. The position drop after the hose rupture in scenario B is greater than in scenario A. This is because gravity is an assisting load in Q_{II}. As shown in Figure 10c and 10d, p_{pa} is controlled at 15 bar by PSV_3 in Q_{II}, and p_a is controlled at 15 bar by PSV_1 in Q_{III}. The load-holding valves are opened by these pressures accordingly. After the hose ruptures on

Preprints.org (www.preprints.org) | NOT PEER-REVIEWED | Posted: 11 April 2024 doi:10.20944/preprints202404.0809.v1

the high-pressure side, p_{pb} drops to zero immediately, and severe oscillations are triggered in p_{a} and p_{b}. However, these oscillations gradually cease after a transition period.

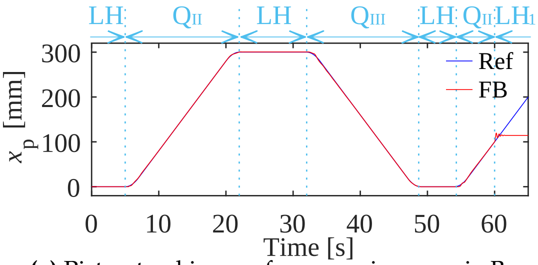

(a) Piston tracking performance in scenario B.

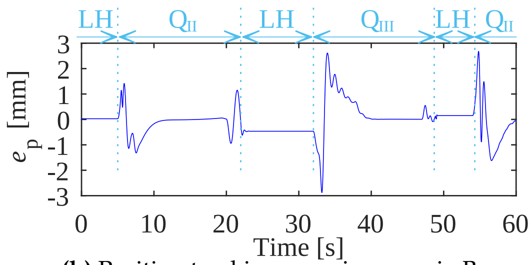

(b) Position tracking error in scenario B.

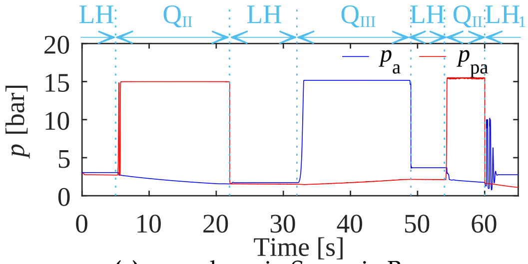

(c) p_{a} and p_{pa} in Scenario B.

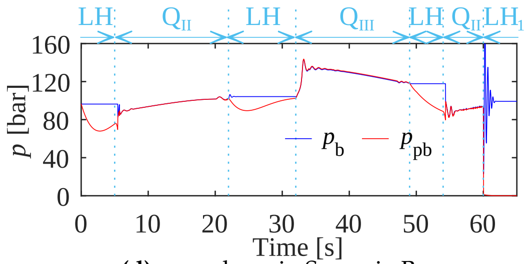

(d) p_{b} and p_{pb} in Scenario B.

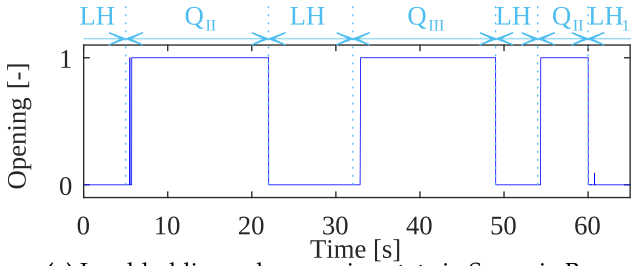

(e) Load-holding valve opening state in Scenario B.

Figure 10. Simulation results in scenario B.

5.3. System Energy Efficiency and PSV Losses

The energy efficiency calculation is only conducted in scenario A. The total power input (P_{M}) is derived via Equation 43. ω is the shaft velocity of M. T_{e} is the effective shaft torque, including the servo motor energy efficiency (η_{M}). T_{e} is calculated via Equation 44. The total output power of the cylinder (P_{C}) is calculated via Equation 45.

$$P_{\mathrm{M}} = \omega T_{\mathrm{e}} \tag{43}$$

$$T_{\mathrm{e}} = \begin{cases} \frac{T_{\mathrm{th}}+T_{\mathrm{s}}}{\eta_{\mathrm{M}}} & \text{in } \mathrm{Q_I} \\ (T_{\mathrm{th}} - T_{\mathrm{s}})\eta_{\mathrm{M}} & \text{in } \mathrm{Q_{IV}} \end{cases} \tag{44}$$

$$P_{\mathrm{C}} = (F_{\mathrm{cyl}} - F_{\mathrm{f}})\dot{x}_{\mathrm{p}} \tag{45}$$

$$\eta_{\mathrm{sys}} = \begin{cases} \frac{P_{\mathrm{C}}}{P_{\mathrm{M}}} & \text{in } \mathrm{Q_I} \\ \frac{P_{\mathrm{M}}}{P_{\mathrm{C}}} & \text{in } \mathrm{Q_{IV}} \end{cases} \tag{46}$$

P_{M} and P_{C} in scenario A is illustrated in Figure 11a. In $\mathrm{Q_I}$, P_{M} is greater than P_{C}. P is in pumping mode. The energy is transferred from M to the cylinder. In $\mathrm{Q_{IV}}$, P_{C} is greater than P_{M}. P is in motoring mode. The energy is transferred from the cylinder to M. In load-holding mode, P_{C} is zero because the piston speed is zero. P_{M} is slightly over zero because the bore-side line pressure needs to be maintained at a certain level. The system energy efficiency (η_{sys}) is calculated via Equation 46. The resulting η_{sys}, depicted in Figure 11b, is obtained after mitigating noise and transition oscillations. In quadrant $\mathrm{Q_I}$, η_{sys} is approximately 66 %, indicating a relatively efficient energy transfer from M to the

Preprints.org (www.preprints.org) | NOT PEER-REVIEWED | Posted: 11 April 2024 doi:10.20944/preprints202404.0809.v1

cylinder. In contrast, in Q_{IV}, η_{sys} is approximately 41 %, suggesting a lower efficiency when the energy is regenerated from the cylinder to M.

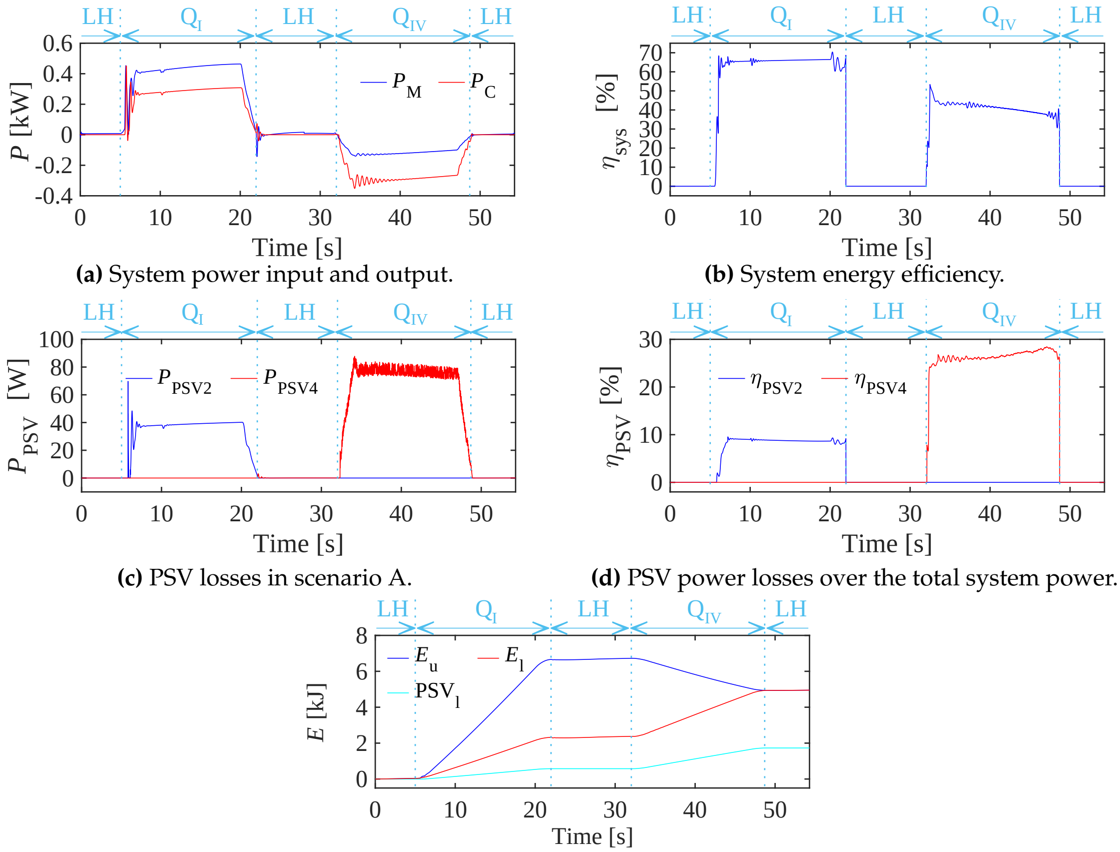

(a) System power input and output.

(b) System energy efficiency.

(c) PSV losses in scenario A.

(d) PSV power losses over the total system power.

(e) Total energy used and total energy losses.

Figure 11. Energy performance in scenario A.

The hydraulic power losses in the PSVs can be calculated by multiplying the pressure drop across the PSVs by the flow rates through the PSVs. PSV_2 and PSV_4 operate in scenario A. Their power losses (P_{PSV2} and P_{PSV4}) are illustrated in Figure 11c. The power loss caused by PSV_2 in Q_I is approximately 39 W. The power loss caused by PSV_4 in Q_{IV} is approximately 77 W. The disparity in power losses between the two PSVs can be attributed to the different flow rates resulting from the differential areas of the cylinder. Figure 11d provides the representation of PSV power losses as a percentage of the total system power. Notably, around 8 % of the power transferred from M to the cylinder is dissipated in PSV_2 in Q_I. Furthermore, approximately 26 % of the power transferred from the cylinder to M is lost in PSV_4 in Q_{IV}. It is important to note that the power losses in PSVs remain constant regardless of the load magnitude. Consequently, the percentages of power losses attributed to the PSVs decrease when the load is larger.

The total energy used (E_u), total energy losses (E_l), and total PSV losses (PSV_l) are shown in Figure 11e. E_u is calculated by integrating P_M. E_l is calculated by integrating the absolute difference between P_M and P_C. PSV_l is calculated by integrating P_{PSV2} and P_{PSV4}. Due to energy regeneration, E_u decreases in Q_{IV}. In contrast, E_l increases in both Q_I and Q_{IV}, eventually equaling E_u. The total PSV losses, PSV_l, exhibit a similar trend to E_l and account for 35 % of E_l.

6. Discussion

The proposed 1M1P MCC can realize the system pressure control, four-quadrant operation, and passive load-holding function triggered by emergencies, such as power loss and hose rupture. Furthermore, it can be deployed in remote installation [12], where the 1M1P MCC Drive Unit and

Preprints.org (www.preprints.org) | NOT PEER-REVIEWED | Posted: 11 April 2024 doi:10.20944/preprints202404.0809.v1

the Cylinder with Passive Load-Holding Device are installed separately and connected via pipelines. Compared with the 2M2P MCC proposed in [18], which can offer the same functionalities, 1M1P MCC has disadvantages and advantages.

As described in Section 5.3, the PSVs in the 1M1P MCC cause energy losses ranging from 8 % to 26 %, depending on the specific operational conditions. These losses are due to the throttling losses in the PSVs. It is important to note that the energy losses in PSVs remain independent of the output powers. Additionally, in scenario A, the highest working pressure is below 60 bar, considerably lower than typical industrial applications. Consequently, with increased load and output power, the proportion of PSV losses is expected to significantly diminish. In contrast, there are no throttling losses in the 2M2P MCC investigated in [18]. This 2M2P MCC uses the same load-holding circuit. Therefore, in theory, it has higher system energy efficiency than the proposed 1M1P MCC. Additionally, since no valves are required to compensate for the cylinder differential flow rate, the issue of pump mode oscillation does not arise in 2M2P MCCs.

The proposed 1M1P MCC surpasses the 2M2P MCC in [18] due to its superior suitability for four-quadrant operations. In the proposed 1M1P MCC, the electric servo motor and hydraulic pump/motor unit effectively contribute to the cylinder's output power in Q_{I} and Q_{III} or engage in power regeneration in Q_{II} and Q_{IV}. In contrast, the 2M2P MCC's secondary electric servo motor and hydraulic pump/motor unit can only contribute to the cylinder's output power in Q_{I} or engage in power regeneration in Q_{IV} [18]. Additionally, the secondary electric servo motor's rated power in the 2M2P MCC must be greater than the main electric servo motor's power due to the system pressure control [18]. Consequently, when significant cylinder output power in Q_{III} is required, an applicable 2M2P MCC becomes more costly and significantly larger than a 1M1P MCC. Therefore, the 2M2P MCC is more suitable for operations only in Q_{I} and Q_{IV}.

7. Conclusions

Realizing a fully hydraulically driven passive load-holding function coping with standstill command, power blackout, and hose rupture presents significant challenges in a regular 1M1P MCC. This paper proposes a novel 1M1P MCC to overcome these challenges through the following key aspects:

- A novel 1M1P MCC with a fully hydraulically driven passive load-holding function was implemented in simulations on a laboratory single-boom crane. The system's operation and passive load-holding modes in all four quadrants and its capability to mitigate pump mode oscillation were extensively analyzed.
- A dynamic model of the proposed 1M1P MCC was developed, and a control algorithm was designed. This control algorithm consists of three control loops to achieve precise control over the piston position and system pressures and a smooth transition between different modes.
- The position tracking error is within ± 2 mm in Q_{I} and Q_{IV}, and within ± 3 mm in Q_{II} and Q_{III}. The error peaks occur during the transition between the operation and load-holding modes. The system pressure to open the load-holding valves is well controlled at around 15 bar. The load-holding function is performed under standstill command, power blackout, and hose rupture situations.
- The overall system energy efficiency is about 66 % when the hydraulic pump/motor unit is in pumping mode (Q_{I}), and 41 % when the hydraulic pump/motor unit is in energy regeneration mode (Q_{IV}). PSVs cause around 8 % energy loss in Q_{I} and around 26 % energy loss in Q_{IV}.
- The advantages and disadvantages of the proposed 1M1P MCC are discussed in comparison to a 2M2P MCC with equivalent functionality. It is found that the proposed 1M1P MCC is more suitable than the 2M2P MCC for four-quadrant operations. However, the inclusion of PSVs in the proposed 1M1P MCC leads to a minor level of energy losses.

In conclusion, the simulation results presented in this paper verify the effectiveness of the functionality of the 1M1P MCC and the proposed control algorithm. This technique holds promise for various industrial applications, particularly those necessitating four-quadrant operation and seamless transitions between motion and load-holding modes, such as industrial cranes and pitch angle control systems for wind turbines. Future work will cover the coupling analysis between the position control and the system pressure control and the experimental test to verify the simulation results.

Author Contributions: Conceptualization, W.Z.; methodology, W.Z.; software, W.Z.; investigation, W.Z.; data curation, W.Z.; writing—original draft preparation, W.Z.; writing—review and editing, W.Z., M.K.E., M.R.H.; supervision, M.K.E., M.R.H., T.O.A.; funding acquisition, M.K.E. All authors have read and agreed to the published version of the manuscript.

Funding: This research was funded by the Research Council of Norway, SFI Offshore Mechatronics, project number 237896/O30.

Conflicts of Interest: The authors declare no conflict of interest.

References

1. Backé, W. Hydraulic Drives with High Efficiency. *Fluid Power Systems and Technology ASME* **1995**, *2*, 45–73.
2. Ding, R.; Zhang, J.; Xu, B.; Cheng, M. Programmable hydraulic control technique in construction machinery: Status, challenges and countermeasures. *Automation in Construction* **2018**, *95*, 172–192. https://doi.org/10.1016/j.autcon.2018.08.001.
3. Liang, X.; Virvalo, T.; Linjama, M. The influence of control valves on the efficiency of a hydraulic crane. In Proceedings of the Sixth Scandinavian International Conference on Fluid Power, Tampere, Finland, 1999, pp. 381–394.
4. Zhao, W.; Ebbesen, M.K.; Andersen, T.O. Identifying The Future Research Trend for Using Speed-Controlled Hydraulic Cylinders in Offshore Applications through Literature Survey. In Proceedings of the 2022 IEEE Global Fluid Power Society PhD Symposium, Naples, Italy, 2022.
5. Hagen, D.; Padovani, D.; Choux, M. A comparison study of a novel self-contained electro-hydraulic cylinder versus a conventional valve-controlled actuator-part 2: Energy efficiency. *Actuators* **2019**, *8*. https://doi.org/10.3390/ACT8040078.
6. Ahn, K.K.; Yoon, J.I.; Truong, D.Q. Design and verification of a new energy saving electric excavator. In Proceedings of the 28th International Symposium on Automation and Robotics in Construction, ISARC 2011, Seoul, Korea, 2011, pp. 259–264.
7. Zhang, S.; Minav, T.; Pietola, M. Decentralized Hydraulics for Micro Excavator. In Proceedings of the 15th Scandinavian International Conference on Fluid Power, Linköping, Sweden, 2017, pp. 187–195.
8. Hagen, D.; Padovani, D.; Choux, M. A comparison study of a novel self-contained electro-hydraulic cylinder versus a conventional valve-controlled actuator-part 1: Motion control. *Actuators* **2019**, *8*. https://doi.org/10.3390/ACT8040079.
9. Parker, H. Electro-Hydraulic Actuators for High Power Density Applications. [EB/OL]. https://www.parker.com/content/dam/Parker-com/Literature/Hydraulic-Pump-Division/Oildyne-EHA/Compact-EHA-Catalog-HY22-3101E-7-13.pdf (Accessed July 07, 2023).
10. Rexroth, B. Self-Contained Actuator for a Variety of Applications. [EB/OL]. https://dc-mkt-prod.cloud.bosch.tech/us/en-2/company/press/cytromotion-compact-hydraulic-actuator-2561.pdf (Accessed July 07, 2023).
11. Thomson. Self-Contained, Electro-Hydraulic Cylinders Improve Power Density and Shock Load Resistance. [EB/OL]. https://www.thomsonlinear.com/en/support/articles/Self-Contained-Electro-Hydraulic-Cylinders-Improve-Power-Density-and-Shock-Load-Resistance (Accessed July 07, 2023).
12. Zhao, W.; Bhola, M. Comparing Compact and Remote Deployments of a Speed-Controlled Cylinder Drive Unit on an Offshore Knuckle Boom Crane. In Proceedings of the 18th Scandinavian International Conference on Fluid Power, Tampere, Finland, 2023.
13. Jalayeri, E.; Imam, A.; Tomas, Z.; Sepehri, N. A throttle-less single-rod hydraulic cylinder positioning system: Design and experimental evaluation. *Advances in Mechanical Engineering* **2015**, *7(5)*. https://doi.org/10.1177/1687814015583249.
14. Imam, A.; Rafiq, M.; Jalayeri, E.; Sepehri, N. Design, implementation and evaluation of a pump-controlled circuit for single rod actuators. *Actuators* **2017**, *6*, 10–16. https://doi.org/10.3390/act6010010.
15. Jensen, K.J.; Ebbesen, M.K.; Hansen, M.R. Novel concept for electro-hydrostatic actuators for motion control of hydraulic manipulators. *Energies* **2021**, *14*. https://doi.org/10.3390/en14206566.

doi:10.20944/preprints202404.0809.v1

16. Padovani, D.; Ketelsen, S.; Hagen, D.; Schmidt, L. A self-contained electro-hydraulic cylinder with passive load-holding capability. *Energies* **2019**, *12*. https://doi.org/10.3390/en12020292.
17. Ketelsen, S.; Andersen, T.O.; Ebbesen, M.K.; Schmidt, L. A Self-Contained Cylinder Drive with Indirectly Controlled Hydraulic Lock. *Modeling, Identification and Control: A Norwegian Research Bulletin* **2020**, *41*, 185–205. https://doi.org/10.4173/mic.2020.3.4.
18. Zhao, W.; Bhola, M.; Ebbesen, M.K.; Andersen, T.O. A Novel Control Design for Realizing Passive Load-Holding Function on a Two-Motor-Two-Pump Motor-Controlled Hydraulic Cylinder. *Modeling, Identification and Control* **2023**, *44*, 125–139. https://doi.org/10.4173/mic.2023.3.3.
19. Williamson, C.; Ivantysynova, M. The Effect of Pump Efficiency on Displacement-Controlled Actuator Systems. In Proceedings of the Eighth Scandinavian International Conference on Fluid Power, Tampere, Finland, 21-23 May 2007.
20. Hansen, A.H. *Fluid Power Systems – A Lecture Note in Modelling, Analysis and Control*; Springer Nature Switzerland AG, 2023.